Journal of *Marine Science and Engineering*

MDPI

Article

Numerical Investigation on Vortex-Induced Vibrations of Two Cylinders with Unequal Diameters

Yangyang Gao [1,2,*], Sisan Yang [1,2], Lizhong Wang [1,2], Caiyun Huan [3,4] and Jie Zhang [3,4]

[1] Ocean College, Zhejiang University, Zhoushan 316021, China
[2] Hainan Institute, Zhejiang University, Sanya 572025, China
[3] Key Laboratory of Far-Shore Wind Power Technology of Zhejiang Province, Hangzhou 311122, China
[4] Renewable Energy Engineering Institute, Power China Huadong Engineering Corporation Limited, Hangzhou 311122, China
* Correspondence: yygao@zju.edu.cn

Abstract: A series of numerical simulations of two-degree-of-freedom vortex-induced vibration of two coupled cylinders with unequal diameters are performed at the Reynolds number of 20,000. The effects of incident angle, spacing ratio, and diameter ratio on the VIV responses for two cylinders are investigated. It is shown that the lock-in range of the large cylinder is significantly widened and the maximum vibration amplitude decreases as a result of the existence of small cylinder. The mean drag coefficients and root mean square force coefficients of the large cylinder are not varied significantly with the incident angle and diameter ratio, but the force coefficients of the small cylinder vary considerably under different configurations. For the configuration of $\alpha = 0°$, $d/D = 0.05$ and $G/D = 0.05$, the variations in vibration amplitude and frequency ratio are similar to those of the isolated cylinder. Different vortex shedding modes such as 2S mode, P+S mode, and 2P mode are observed for two coupled cylinders at different reduced velocities for different configurations.

Keywords: two coupled cylinders with unequal diameters; vortex-induced vibration; diameter ratios; incident angles; vibration response; vortex shedding modes

Citation: Gao, Y.; Yang, S.; Wang, L.; Huan, C.; Zhang, J. Numerical Investigation on Vortex-Induced Vibrations of Two Cylinders with Unequal Diameters. *J. Mar. Sci. Eng.* **2023**, *11*, 377. https://doi.org/10.3390/jmse11020377

Academic Editor: Unai Fernandez-Gamiz

Received: 7 January 2023
Revised: 1 February 2023
Accepted: 2 February 2023
Published: 8 February 2023

1. Introduction

As oil and gas exploration extends to deep and ultra-deep water, the technological challenges of the riser system increase rapidly [1]. An important issue for the riser system is the fatigue failure caused by the vortex-induced vibration (VIV). A real-time and effective monitoring device is urgently needed to monitor the VIV of riser. Due to the advantages of multi-parameters, high capacity and accuracy, low cost, easy deployment, and realization of long-distance monitoring, the fiber optic sensing cables bundled together with the riser can achieve the real-time monitoring of the VIV of riser. However, due to the proximity interference between the cable and riser, the dynamic responses of vortex-induced vibration for the coupled riser-cable system are much more complicated than that of an isolated riser.

Over the past few decades, the investigation of the vortex-induced vibration for a single elastically mounted cylinder has been extensively conducted [2–5]. Feng [6] and Williamson et al. [7] experimentally investigated one-degree-of-freedom (1-DOF) vortex-induced vibration of a single cylinder. The initial branching, upper branching, and lower branching were observed with the variation in reduced velocity, while the lock-in and hysteresis phenomena were demonstrated. Verma and De [8] numerically investigated the two-degree-of-freedom (2-DOF) VIV of an elastically mounted circular cylinder. Two branches (Initial Branch, Lower Branch) and three branches (Initial Branch, Upper Branch, Lower Branch) amplitude responses were observed for the low and high Re values, respectively. It was found that the dynamic responses and wake flow patterns of two-degree-of-freedom (2-DOF) VIV have a more complicated behavior than those of 1-DOF vortex-induced vibrations [2,9,10].

The investigation of vortex-induced vibration of two cylinders have drawn considerable attention. Borazjani and Sotiropoulos [11] conducted the numerical investigations of VIV for two tandem cylinders with equal diameter at Re = 200. It was found that the gap flow between two cylinders induces the pressure gradients, resulting in significant oscillatory forces in phase with the vortex shedding. Ping et al. [12] studied the transverse VIV of two coupled cylinders in a tandem arrangement. It was found that the gap flow appearing in the lower branch can lead to complex vortex-to-body and vortex-to-vortex interactions that substantially alter the VIV response. Papaioannou et al. [13] investigated the effect of spacing ratio on the 2-DOF vortex-induced vibration of two tandem cylinders for Re = 160, where the spacing ratio plays an important role in the synchronization region of the upstream cylinder. The maximum amplitude and synchronization range of the downstream cylinder increase with a decrease in spacing ratio. Chung [14] numerically investigated the 2-DOF VIV of two identical spring-supported cylinders with the mass ratio of 2 and Re =100. The streamwise amplitude is generally comparable to the transverse amplitude and is accompanied by with irregular trajectories. Chen et al. [15] conducted the numerical simulations of the VIV of two cylinders in side-by-side configuration at Re = 100 using the immersed boundary method. The dynamic response of the cylinders can be divided into four different branches. The asymmetric in-flow vibrations are observed at $4.0 < U_r < 4.4$ for $L/D = 2.5$ (L is the center-to-center distance between two cylinders). Chen et al. [16] numerically studied the FIV of two side-by-side circular cylinders for the Reynolds number of 60–200. The phase jump between the lift and displacement is related to the presence of multiple harmonic frequencies, which is different from that of an isolated cylinder.

The complex interference between two cylinders with unequal diameters undergoing VIV has been extensively studied. Zang [17] performed a series of experiments using particle image velocimetry (PIV) to investigate the VIV of piggyback pipelines in the subcritical flow regime. For $G/D \geq 0.3$, the effect of the piggyback could be ignored due to the weak interaction between two pipelines. Zang and Gao [18] experimentally investigated the effects of diameter ratios, gap ratios, and incident angles on the VIV responses of piggyback pipelines. The results show that the VIV is suppressed significantly for $G/D = 0.25$ and $\alpha = 90^\circ$. The lock-in regime and vibration amplitude of two piggyback pipelines are greatly influenced by the incident angle. Assi [19] investigated the wake-induced vibration of the downstream cylinder for different diameter ratios of $0.33 \leq D_1/D_2 \leq 1$ (D_1 and D_2 represent the diameters of the upstream and downstream cylinders, respectively). The transverse amplitudes reach $1.5D$ at high reduced velocity range outside the lock-in region. Moreover, the transverse displacement of the upstream cylinder becomes larger than that of downstream cylinder when the spacing ratio reaches a relatively small value. Zhao et al. [20] carried out the numerical investigation of flow past two side-by-side cylinders with unequal diameters at low Reynolds numbers based on the finite element method. Three types of vortex shedding modes were observed and classified as a single-wake shedding mode, interaction mode, and two-wake mode as the gap ratio increased.

The above-mentioned studies are mostly focused on the VIV of two cylinders with equal diameter in the low Reynolds number regime. However, the dynamic response and vortex shedding pattern of coupled two cylinders with unequal diameters are not well-understood. Zhu et al. [21] investigated the flow-induced vibration (FIV) of two rigidly coupled tandem cylinders with unequal diameters at $Re = 150$, the results indicate that the flow regime transition was sensitive to the gap ratio and the reduced velocity. Zhao et al. [22] investigated the 1-DOF VIV of two coupled cylinders with equal diameter in tandem and side-by-side configurations in the cross-flow direction. They found that the maximum vibration amplitude occurs in the lock-in range at $G/D = 0.5$ (G is the gap between two cylinders, D is the diameter of the cylinder) in side-by-side configuration, and the maximum value is approximately twice that of a single cylinder. Zhao and Yan [23] conducted the investigation focused on the effect of incident angle α on the lock-in regime of VIV for two cylinders with unequal diameters using the Petrov–Galerkin Finite Element

Method (PG-FEM). The results show that the lock-in range is expanded considerably. The 2-DOF VIV of two coupled cylinders at d/D = 0.1 was investigated numerically by Rehmanian et al. [24]. The vibration frequency component, vibration amplitude, and force coefficient are sensitive to the incident angle and gap ratios. The largest vibration amplitudes in the cross-flow and in-line directions both occur at $\alpha = 67.5^\circ$ and G/D = 0.1. The lock-in regime and vibration frequency of small cylinder are consistent with that of the large cylinder [25]. Serta and Janocha [26] performed the numerical simulation of 2-DOF flow-induced vibration of two coupled cylinders at Re = 3.6×10^6, the extended lock-in range is observed at G/D = 0.1 with the incident angles of $\alpha = 90^\circ$ and 180°. The motion trajectories and vortex shedding patterns behave more irregularly at $\alpha = 90^\circ$. Ping et al. [27] numerically investigated the VIV of two rigidly connected cylinders of unequal diameters at Re = 250 and d/D = 0.2. The structural dynamic responses and hydrodynamic forces are strongly depended on the configurations.

As mentioned above, few investigations have been performed for vortex-induced vibrations of two coupled cylinders with unequal diameters, especially at subcritical Reynolds numbers. The purpose of the present study is to investigate the 2-DOF VIV of two coupled cylinders with unequal diameters to optimize the configuration of coupled riser-cable systems. The effects of incident angle, spacing ratio, and diameter ratio on the VIV response and vortex shedding mode of two coupled cylinders are further analyzed. The paper is organized as follows. In Section 2, the numerical method and validation are described in detail. In Section 3, the numerical results for vibration amplitude, force coefficient, motion trajectory, and wake flow pattern are analyzed. Finally, the conclusions are drawn in Section 4.

2. Numerical Method

2.1. Governing Equations

Two-dimensional models based on RANS equations have been demonstrated to predict the response amplitudes and frequencies of VIV with sufficient accuracy [4,24,28]. Flow past two coupled cylinders with unequal diameters is governed by the unsteady two-dimensional incompressible RANS equations:

$$\frac{\partial u_i}{\partial x_i} = 0 \tag{1}$$

$$\frac{\partial u_i}{\partial t} + \frac{\partial}{\partial x_j}(u_i u_j) = -\frac{1}{\rho}\frac{\partial p}{\partial x_i} + \frac{1}{\rho}\frac{\partial}{\partial x_j}\left(\mu\frac{\partial u_i}{\partial x_j} - \rho\overline{u_i u_j'}\right) \tag{2}$$

where u_i denotes the fluid velocity in x_i-direction, ρ is density of the fluid, p is the pressure, μ denotes the kinematic viscosity, and $\overline{u_i' u_j'}$ denotes the Reynolds stress tensor.

The riser and fiber optic cable are rigidly coupled together, assumed as two coupled cylinders with unequal diameters. Moreover, the equations of motions of two coupled cylinders system are expressed as follows:

$$m\ddot{x} + c\dot{x} + kx = F_x \tag{3}$$

$$m\ddot{y} + c\dot{y} + ky = F_y \tag{4}$$

where m, c, and k denote the mass, damping, and stiffness of the two coupled cylinders system, respectively. x and y denote the streamwise and transverse displacement, respectively. F_x and F_y are the fluid forces in the streamwise and transverse directions, respectively.

In the present study, the Shear Stress Transport (SST) $k-\omega$ turbulence model is used for simulating the VIV of two coupled cylinders. A sufficiently fine mesh is adopted to ensure the accurate numerical simulation of near-wall flow. The distance of the first layer on the surface of the cylinder defined as $y^+ = \mu_f \Delta y/\nu$ is less than 1, where μ_f is the friction

velocity and Δy is the radial distance between the nodes of the first layer mesh and cylinder surface.

The RANS equations are solved using the Open-Source Field Operation and Manipulation (OpenFOAM®v1806), which is a free, open source CFD software developed primarily by OpenCFD Ltd. The pressure implicit with splitting of operator (PISO) method and pimpleFoam solver are used to solve the coupling of pressure and velocity. The second-order backward implicit Euler scheme is used for the time integration. The convection terms are discretized using the Gauss linear scheme. The linear scheme and Gauss linear corrected are used to discretize the interpolation and Laplacian terms, respectively. The Newmark-β method is used to solve the equations of motion for the elastically mounted cylinder system. The dynamicFvMesh is used for the two-degree-of-freedom motions of the system. The quality and effectiveness of the mesh are controlled by the motionDirectional diffusion model.

2.2. Computational Set Up

The schematics of the 2-DOF VIV of two coupled cylinders with unequal diameters are shown in Figure 1. The computational domain of the numerical simulation for two coupled cylinders is $45D \times 30D$. For the purpose of convenience, the large and small cylinders are labeled as $C1$ and $C2$, respectively. The inlet boundary is located $15D$ upstream from the center of $C1$ and the outlet is placed $30D$ downstream from the center of $C1$. The distance between the top and bottom boundaries and the center of $C1$ are $15D$. On the inlet boundary, the Neumann condition is used for pressure. The flow velocity is set to be $u_x = U$ and $u_y = 0$. The turbulent kinetic energy k and specific dissipation ω are provided as $k = 1.5(UI)^2$ and $\omega = k^{0.5}/\left(C_\mu^{0.25} l\right)$, respectively, where the turbulence intensity I is 0.9% [29], the model constant is $C_\mu = 0.09$, and the turbulence length scale l is set to $0.04D$ [30]. On the outlet boundary, the pressure is set to zero and the normal gradients of the velocity, k and ω, are zero. The no-slip condition is employed on the surfaces of two cylinders, $k = 0$ and $\omega = 60\nu/\left(0.075\Delta x^2\right)$, where Δx is the distance between the cylinder surface and the first layer of computational nodes. The symmetry condition is adopted on the top and bottom boundaries.

The mass ratio is $m^* = 2.0$ and the damping coefficient for two coupled cylinders is zero in the present study. The incoming flow velocity is 0.2 m/s, corresponding to the Reynolds number of 20,000. The diameter ratio d/D and spacing ratio G/D are varied from 0.05 to 0.3, respectively. For the examined configurations, d/D and G/D, are kept consistent. The incident angle α is chosen to be 0°, 90°, and 180°. The reduced velocity U_r is varied in the range of 2 to 14.

2.3. Numerical Validation and Mesh Dependency Study

To validate the accuracy of present numerical model, comparisons of the 2-DOF VIV of an isolated cylinder from the present numerical simulation with reported experiment and numerical results were performed. In the numerical validation, the simulation parameters were kept consistent with those used in the experiment of Jauvtis and Williamson [2], $D = 0.0381$ m, $m^* = 2.6$, $\xi = 0.003611$ and the natural frequency $f_n = 0.4$, the Reynolds number varied from 1500 to 10,000.

The variations in the streamwise and transverse vibration amplitudes and the ratios of transverse vibration frequency to natural frequency with reduced velocities are shown in Figure 2. The results well capture the initial branching, upper branching, and lower branching. The variations in the transverse vibration amplitude are generally consistent with previous results [2,4,5,31], as well as the ratio of transverse vibration frequency to natural frequency at different reduced velocities. The streamwise and transverse amplitudes are slightly less than the previous results at $6.4 \leq U_r \leq 7$ for the super upper branch. The present results demonstrate that the numerical model is sufficiently accurate for solving the vortex-induced vibration of two coupled cylinders with unequal diameters.

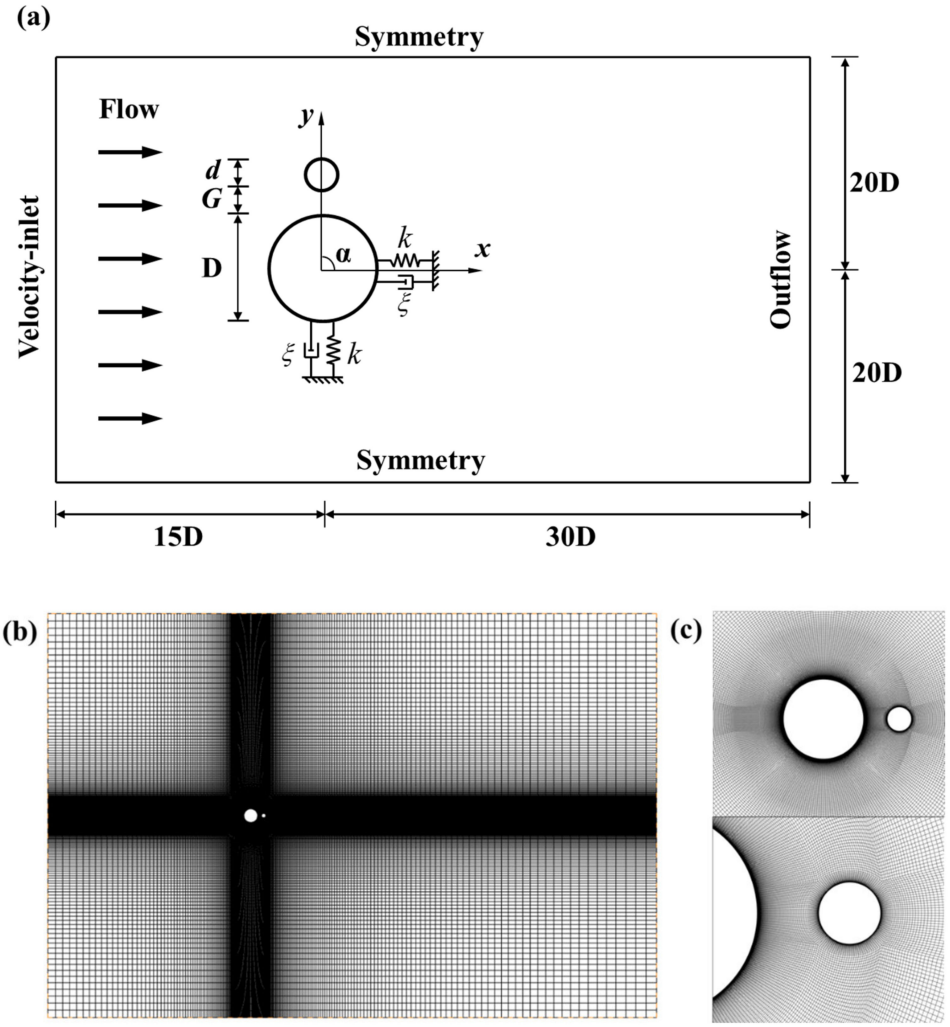

Figure 1. The schematics of computational domain of two coupled cylinders system: (**a**) sketch of the computational model ($\alpha = 90°$); (**b**) computational mesh ($\alpha = 0°$ and $d/D = 0.3$); (**c**) mesh details around two coupled cylinders.

In order to test the mesh and time-step dependency, the numerical simulations of 2-DOF VIV of a single cylinder at Re = 20,000 and $U_r = 5$ were performed. Three meshes with different densities were adopted for the mesh dependency study. Table 1 shows the comparisons of the streamwise and transverse vibration amplitudes, mean drag coefficients, and root mean square lift coefficients of a single cylinder calculated from different meshes. The drag and lift force coefficients and the corresponding root mean square values are defined as follows:

$$C_D = \frac{2F_D}{\rho U^2 A} \tag{5}$$

$$C_L = \frac{2F_L}{\rho U^2 A} \tag{6}$$

$$\overline{C_D} = \frac{1}{n}\sum_{i=1}^{n} C_{D,i} \tag{7}$$

$$C'_D = \sqrt{\frac{1}{n}\sum_{i=1}^{n}\left(C_{D,i} - \overline{C_D}\right)^2} \tag{8}$$

$$C'_L = \sqrt{\frac{1}{n}\sum_{i=1}^{n}\left(C_{L,i} - \overline{C_L}\right)^2} \quad (9)$$

where F_D and F_L denote the drag and lift force on the single cylinder, respectively. ρ and U are the density of the fluid and the incoming flow velocity, respectively, A denotes the projected area of the cylinder in the incoming flow direction.

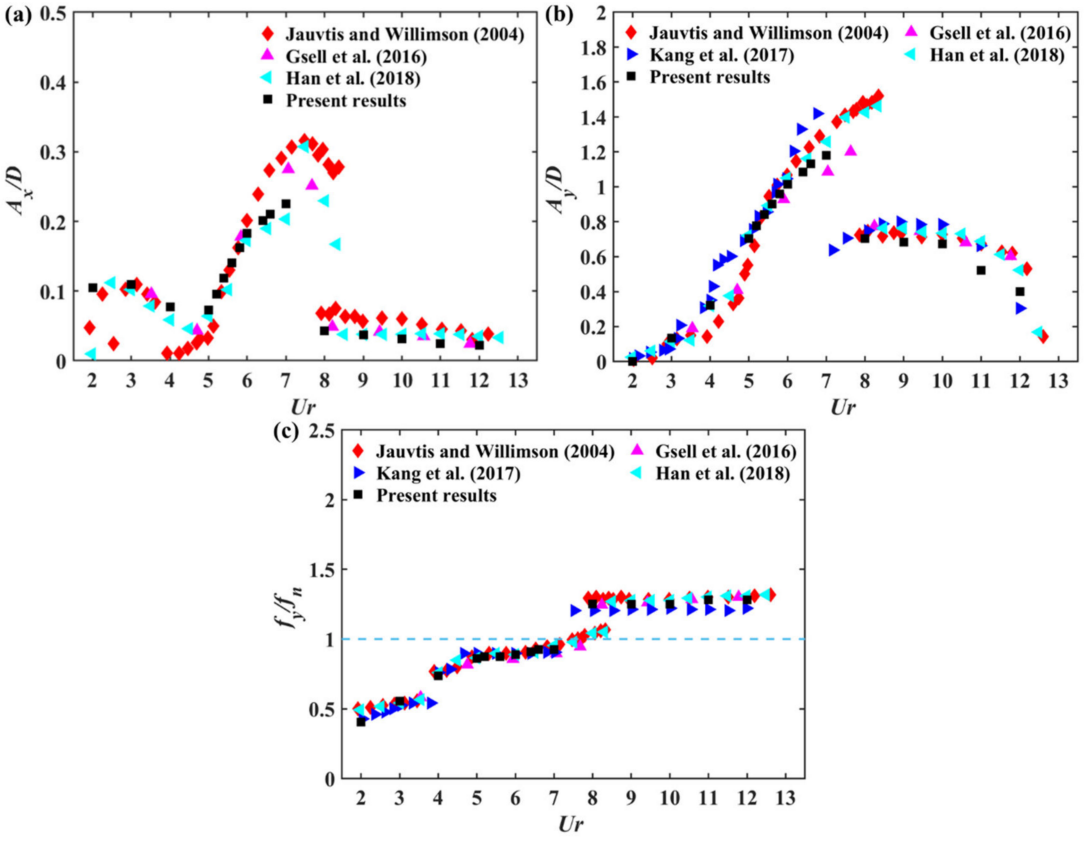

Figure 2. Comparisons of the response amplitudes and frequencies for the VIV of an isolated cylinder at different reduced velocities with references [2,4,5,31]: (**a**) streamwise amplitudes; (**b**) transverse amplitudes; (**c**) frequency ratio in the transverse direction.

Table 1. Mesh dependence for the VIV of an isolated cylinder at Re = 20,000 and U_r = 5.

Mesh	Nodes	Elements	A_x/D	A_y/D	$\overline{C_D}$	C'_L
M1	160	27,552	0.2135	1.0955	2.3328	1.5947
M2	200	34,752	0.2076	1.1088	2.3401	1.5870
M3	240	48,000	0.2081	1.1093	2.3424	1.5861

As can be seen from the comparison of the results between the coarse and medium mesh (M1 and M2) in Table 1, the maximum discrepancies of A_x/D and A_y/D are 2.7% and 1.2%, respectively, which are reduced to only 0.24% and 0.05% compared with the results of M2 and M3, respectively. Moreover, the discrepancies in the values of $\overline{C_D}$ and C'_L between medium mesh and fine mesh are 0.09% and 0.06%, respectively. Therefore, the medium mesh is considered dense enough to obtain precise results for the following simulations. A further study of time-step independence is conducted with four different time sizes based on the medium mesh M2 ($U\Delta t/D$ = 0.002, 0.001, 0.0005, 0.0002). The comparisons of the results are shown in Table 2, it can be seen that the maximum difference in $\overline{C_D}$ between $U\Delta t/D$ = 0.002 and 0.001 is 6.33% and reduces to 0.78% as $U\Delta t/D$ decreases to 0.0005.

Therefore, the non-dimensional computational time step $U\Delta t/D = 0.0005$ is suitable and sufficient for ensuring the convergence and accuracy of the present simulation.

Table 2. Comparisons of results for an isolated cylinder for four different time-step sizes at Re = 20,000 and U_r = 5.

$U\Delta t/D$	A_x/D	A_y/D	$\overline{C_D}$	C_L'
0.002	0.210	1.101	2.518	1.551
0.001	0.207	1.110	2.359	1.575
0.0005	0.208	1.109	2.340	1.587
0.0002	0.207	1.109	2.343	1.583

3. Results and Discussion

3.1. Vibration Amplitudes and Frequencies

Numerical simulations were performed to investigate the effects of incident angle, spacing ratio, and diameter ratio on the VIV of coupled cylinders with unequal diameters. Figure 3 presents the variations in the non-dimensional vibration amplitudes and the ratio of transverse vibration frequency to natural frequency with the reduced velocities at different incident angles and diameter ratios, with the value of diameter ratio and spacing ratio kept constant. It is found that the variations in the vibration amplitudes of two rigidly coupled cylinders with the reduced velocities seem more complicated than that of a single cylinder especially in the range of high reduced velocity. The incident angles and diameter ratios have significant effects on the vibration amplitudes and frequency for two coupled cylinders.

For d/D = 0.3, at the incident angle $\alpha = 0^\circ$, the transverse vibration amplitude of A_y is reduced for $3 \leq U_r \leq 6$ compared with the single cylinder and the maximum value of A_y reaches $1.03D$ for U_r = 7. Moreover, A_x is increased significantly for $7 \leq U_r \leq 14$ and the frequency ratio f_y/f_n varies around 1 for $7 \leq U_r \leq 14$. The comparisons of VIV responses obtained from three different incident angles at a large diameter ratio (d/D = 0.3) were performed. The vibration amplitudes and frequencies at the high reduced velocities range are significantly different regardless of the incident angle, and the increase in diameter of the small cylinder leads to different flow patterns and pressure distributions, resulting in the significant variation in vibration amplitude of the large cylinder. As d/D decreases from 0.3 to 0.1, the variations in streamwise and transverse vibration amplitudes become similar to those of an isolated cylinder. For d/D = 0.1, the transverse vibration amplitude of A_y is increased for $7 \leq U_r \leq 14$ and the maximum value of A_y is equal to $1.07D$ at U_r = 6. The variation in vibration amplitudes with reduced velocities show some similarities to those of the isolated cylinder. The transverse vibration frequency ratio f_y/f_n is constant at 1.15 for $11 \leq U_r \leq 14$. The lock-in ranges for d/D = 0.1 and 0.3 extend beyond U_r = 14. Moreover, as d/D decreases to 0.05, both the streamwise and transverse vibration amplitudes decrease significantly for U_r = 6. The variations in transverse vibration frequency ratio and the lock-in range are consistent with those of the isolated cylinder. For d/D = 0.05, the small cylinder has slight effects on the frequency ratio and vibration amplitude of the large cylinder compared with the large diameter ratios at $\alpha = 0^\circ$.

The normalized Fast Fourier Transform (FFT) amplitude spectra of the transverse displacement are presented as functions of U_r and f_y/f_n in Figure 4. For d/D = 0.3, the peak is not obvious due to the presence of small cylinder, especially at high reduced velocities. Compared with the isolated cylinder, the frequency ratio f_y/f_n for the dominant peak is varied from 0.7 to 1.0 in the lock-in region $7 \leq U_r \leq 14$ at $\alpha = 0^\circ$. Meanwhile, the spectra of the transverse displacement for two coupled cylinders have a wide bandwidth with multiple peak frequencies for $4 \leq U_r \leq 10$. A similar phenomenon is also observed for other incident angles in Figure 4c,d. The appearance of multiple peaks may be caused by the interference between the reattachment of shear layers and shed vortices. The proximity interferences between two coupled cylinders lead to the irregularities of lift force and

vibration amplitude. The peak becomes more obvious with the decrease in d/D compared with that of $\alpha = 0°$. The coupled cylinders can be regarded as a single bluff body for $d/D = 0.05$, and a single distinct peak is generally observed in the power spectrum for the single bluff body mode. As shown in Figure 4f, the frequency ratio f_y/f_n for the dominant peak is varied from 0.8 to 1.2 for $6 \leq U_r \leq 14$. The peak response is different from that of the isolated cylinder at high reduced velocities $11 \leq U_r \leq 14$. For $d/D = 0.05$, the frequency ratio f_y/f_n for the dominant peak is varied from 2.6 to 2.9 for $13 \leq U_r \leq 14$. It can be seen that two coupled cylinders for the configuration of $d/D = 0.05$ and $\alpha = 0°$ exhibit similar features to the isolated cylinder, indicating the weak effect of the small cylinder on the large cylinder.

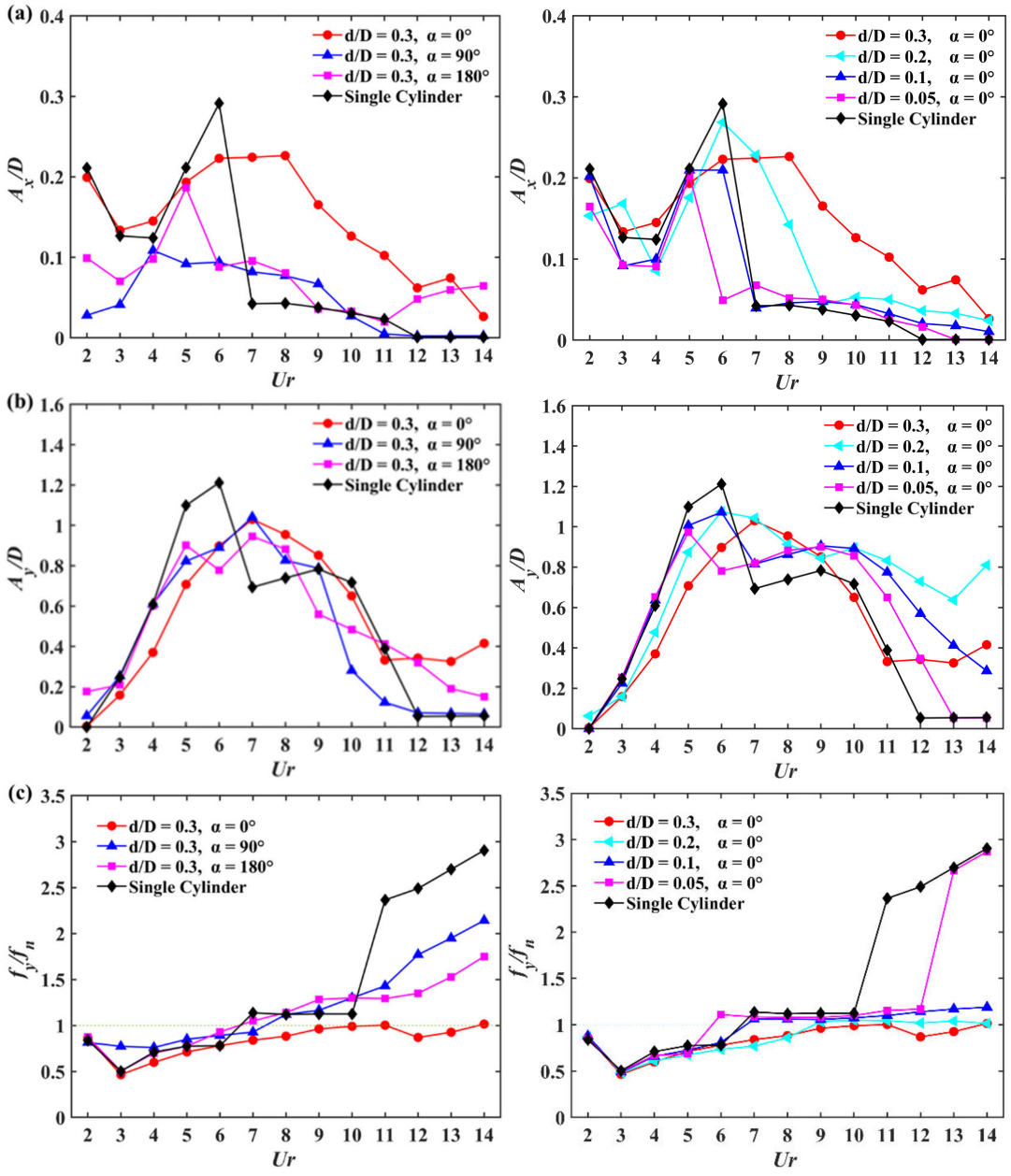

Figure 3. Variations in the non-dimensional vibration amplitudes and frequency ratio with the reduced velocities at different incident angles and diameter ratios: (**a**) streamwise amplitudes; (**b**) transverse amplitudes; (**c**) frequency ratio in the transverse direction.

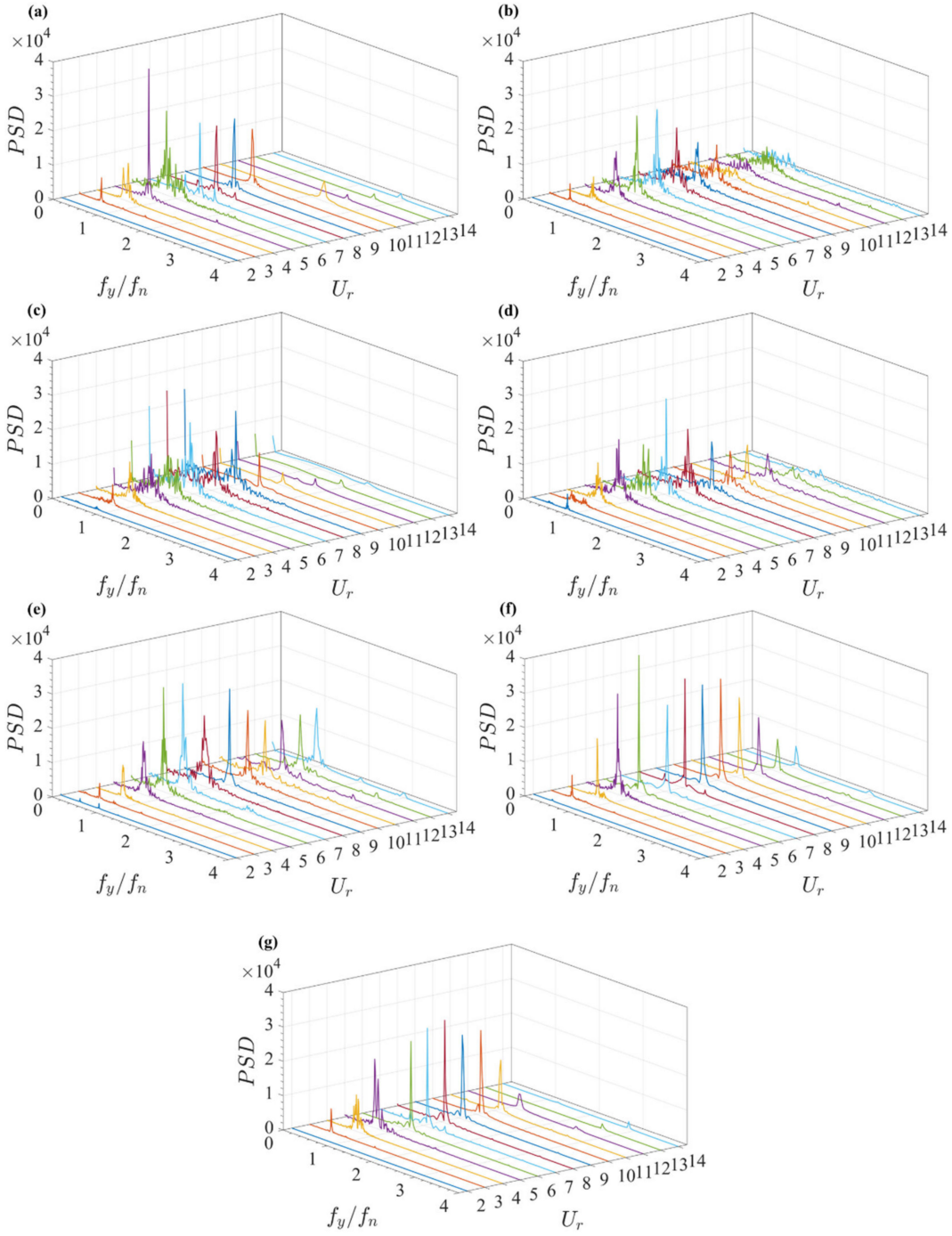

Figure 4. Normalized FFT amplitude spectra of the transverse displacement: (**a**) a single cylinder; (**b**) $\alpha = 0°$, $d/D = 0.3$; (**c**) $\alpha = 90°$, $d/D = 0.3$; (**d**) $\alpha = 180°$, $d/D = 0.3$; (**e**) $\alpha = 0°$, $d/D = 0.2$; (**f**) $\alpha = 0°$, $d/D = 0.1$; (**g**) $\alpha = 0°$, $d/D = 0.05$.

3.2. Force Coefficient

Figure 5 shows the variations in $\overline{C_D}$, C'_D, and C'_L for two coupled cylinders with reduced velocities U_r at different diameter ratios and incident angles. For the configuration of $d/D = 0.3$ at $\alpha = 90°$ and $180°$, the $\overline{C_D}$ of the large cylinder exhibits different behavior from that of the single cylinder at the lock-in range. However, similar variations are observed for different incident angles at large reduced velocities. The $\overline{C_D}$ of the large cylinder is reduced at $3 \leq U_r \leq 6$ and increased at $7 \leq U_r \leq 8$ compared with that of the isolated cylinder. Moreover, the mean drag coefficient $\overline{C_D}$ of the large cylinder reaches the peak value at

U_r = 6 for α = 0° and 180°, consistent with the variation in the single cylinder. Meanwhile, it can be seen that the $\overline{C_D}$ of the small cylinder varies significantly for different incident angles. The large value of $\overline{C_D}$ for the small cylinder is observed in the range of 2.0–2.5 at α = 90°. A significant decreasing in $\overline{C_D}$ is observed at α = 0° and the negative value of $\overline{C_D}$ is observed for U_r = 3 and 11 $\leq U_r \leq$ 14 due to the shielding effect of the large cylinder. A strong backflow is formed in the wake shield region, resulting in a force reversal of the small cylinder. As shown in Figure 5b,c, the variations in C_D' and C_L' for coupled cylinders are more complex especially for 2 $\leq U_r \leq$ 10. For α = 0°, the maximum values of C_D' and C_L' on the large cylinder decrease by 26.2% and 19.4% compared with the isolated cylinder, respectively. Moreover, C_D' of small cylinder *C*2 is significantly larger for 5 $\leq U_r \leq$ 10 compared with other configurations, which may be caused by the disturbances from the unsteady vortex shedding mode of large cylinder. It can be seen that the force coefficients of two coupled cylinders with *d*/*D* = 0.3 vary significantly with different incident angles.

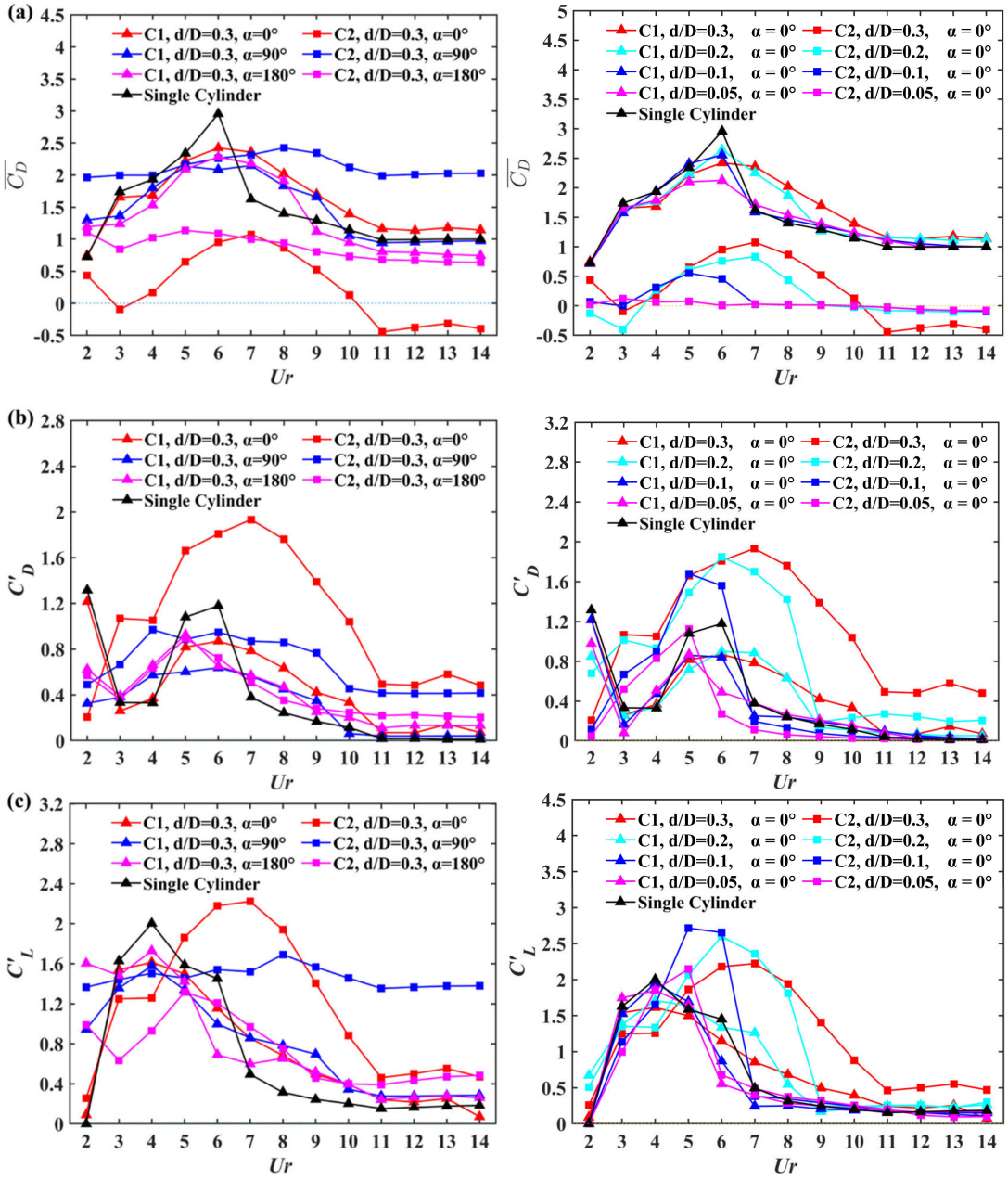

Figure 5. Variations in the force coefficient with the reduced velocity: (**a**) the mean drag coefficient; (**b**) the r.m.s. drag coefficient; (**c**) the r.m.s. lift coefficient.

For $\alpha = 0°$, with the decrease in d/D, the variations in the force coefficients with U_r for the large cylinder are similar to those of the isolated cylinder. As shown in Figure 5a, the mean drag coefficient $\overline{C_D}$ of the large cylinder reaches the peak value at $U_r = 6$ as d/D decreases to 0.1 or 0.05, consistent with that of the isolated cylinder. When d/D decreases to 0.05, the maximum value of $\overline{C_D}$ becomes smaller. Moreover, it is interesting to note that the $\overline{C_D}$ of the small cylinder approaches to 0 for $d/D = 0.05$. For $d/D = 0.1$, although the variations in $\overline{C_D}$ for the large cylinder are most similar to the single cylinder among all configurations, the small cylinder is subject to a certain amount of drag force for $4 \leq U_r \leq 6$ and the values of C_D' and C_L' are kept at larger values for $5 \leq U_r \leq 6$.

The cross-correlation coefficients and phase difference between the transverse displacement and lift force for the large cylinder at different incident angles and diameter ratios are presented in Figure 6. The cross-correlation coefficient $C_{F_L,Y}(\tau)$ of transverse displacement and lift force is calculated, similar to the method used in Gao et al. [32], as follows:

$$C_{F_L,Y}(\tau) = \frac{\overline{\{Y(t)\}\{F_L(t+\tau)\}}}{\left[\overline{\{Y(t)\}^2}\right]^{1/2}\left[\overline{\{F_L(t+\tau)\}^2}\right]^{1/2}} \tag{10}$$

where τ is the time lag. The phase angle φ between the transverse vibration amplitude and lift force is calculated from the phase difference between the peak frequency component of the vibration amplitude and lift force at the same frequency.

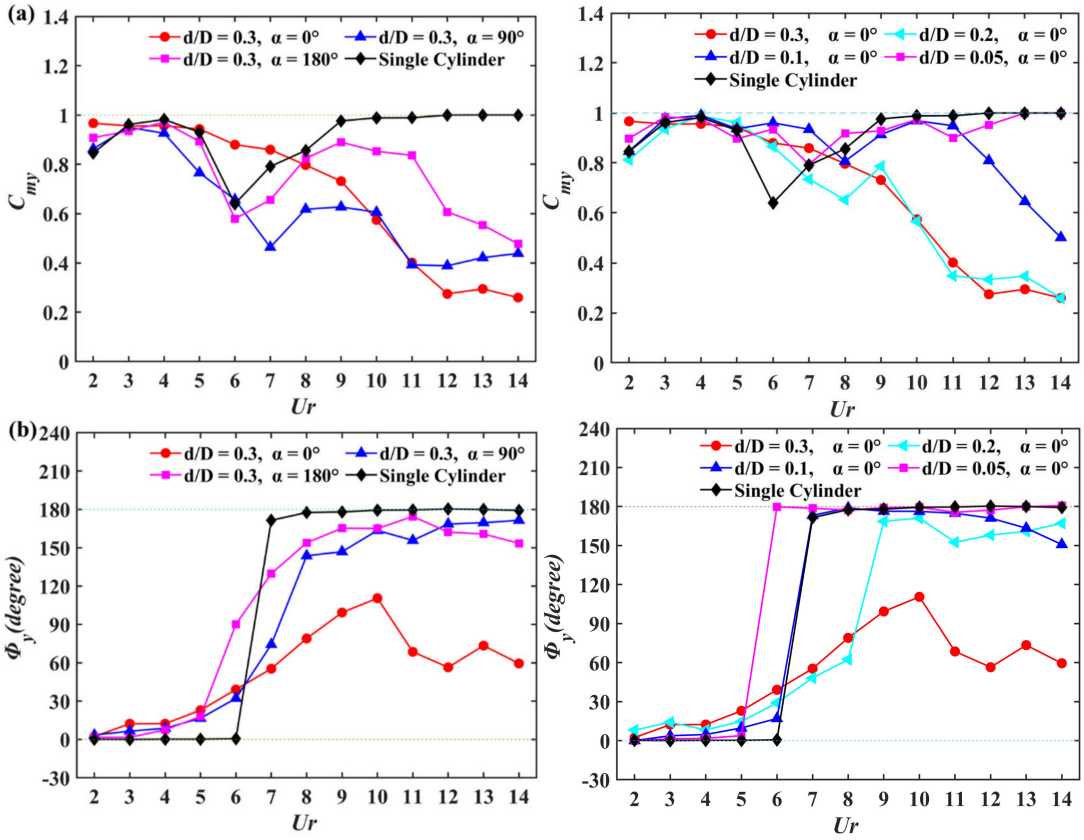

Figure 6. The correlation coefficient and the phase difference between the transverse vibration amplitude and lift force: (**a**) the correlation coefficient; (**b**) the phase difference.

As shown in Figure 6, the correlation coefficient of the isolated cylinder between the transverse vibration amplitude and lift force is about 1 when they are in phase or anti-phase with each other [33], and the minimum value of the maximum correlation coefficient C_{my} reaches to 0.64 for $U_r = 6$. When U_r increases to 7, φ changes from 0° to 170°. The

responses of lift force and transverse displacement are always in the in-phase or anti-phase modes, while the variations in the maximum correlation coefficients are more complicated for two coupled cylinders than that of the isolated cylinder. For d/D = 0.3, when the harmonic of the transverse vibration amplitude and lift force is in anti-phase, the maximum correlation coefficients of two coupled cylinders at different incident angles are smaller than 1. Moreover, the maximum value decreases to about 0.27 at high reduced velocities $U_r \geq 12$ for $\alpha = 0^\circ$. The decrease in the correlation coefficient may be due to the enhancement of nonlinear effects of the vortices shed from two coupled cylinders. The vortices shed from the surfaces of two cylinders are influenced by the gap flow, which may lead to phase variation between the lift force and vibration displacement. As shown in Figure 4b, the peak of the spectra at large reduced velocity is not obvious and the spectra of the transverse displacement for two cylinders are broadband with multiple peak frequencies, which indicates that the variations in the transverse vibration amplitude and lift force are significantly random. Different from the sudden change in the phase for the isolated cylinder at $U_r = 7$, the phase of two coupled cylinders gradually changes at $4 \leq U_r \leq 10$ for $\alpha = 90^\circ$ or $\alpha = 180^\circ$. It is interesting to note that for $\alpha = 0^\circ$, the phase is always in the transition at high reduced velocities and not strictly in-phase or anti-phase. In the VIV of two coupled cylinders, the phase shift between transverse vibration amplitude and lift force for d/D = 0.3 or 0.2 appears to be significantly different from that of the isolated cylinder at different incident angles. For the larger diameter ratio, there is no relatively regular periodic motions in the lock-in region and the corresponding vibration displacement is poorly correlated with the lift force.

As the diameter ratio decreases, the effects of the small cylinder on the correlation coefficients and phase angles of two coupled cylinders become weak for $\alpha = 0^\circ$. The phase angle φ is about 0° for $U_r \leq 6$ and jumps to 180° for $U_r \geq 7$, and there is no transition phase for d/D = 0.3 and $\alpha = 90^\circ$ or 180°. However, both the correlation coefficient and phase angle decrease with U_r for $U_r \geq 12$, which indicates the transverse vibration amplitude and lift force coefficient are not strictly anti-phase. When d/D decreases to 0.05, the minimum value of the correlation coefficient C_{my} is observed at $U_r = 7$, while φ changes from 0° to 180° as U_r increases to 6. At $U_r > 6$, the phase angle φ is about 180°, indicating that the transverse displacement is in anti-phase with the lift force coefficient. It can be seen that as d/D decreases to 0.05, the correlation coefficients and phase angle of two coupled cylinders are almost similar to those of the isolated cylinder.

3.3. Trajectory Response

As shown in Figures 7–10, the X-Y trajectories of the two coupled cylinders are different at different incident angles and diameter ratios. These figures show that the dynamic responses are strongly depended on the incident angle, spacing ratio, and reduced velocity. For the case of $\alpha = 0^\circ$ and d/D = 0.3, the streamwise vibration response is dominant and the transverse vibration amplitude is extremely small at low reduced velocity $U_r = 2$. For $U_r = 3$, the trajectories are chaotic and similar to the shapes of "flat Figure 8", the reason may be attributed to the effect of streamwise vibration on the transverse vibration frequency. With the increase in reduced velocities U_r to 5 and 6, the transverse vibration amplitude becomes dominant. Moreover, the trajectories of two coupled cylinders become more regular, exhibiting the disordered figure of "8".

For the incident angle $\alpha = 90^\circ$ and d/D = 0.3 presented in Figure 8, different from the configuration for $\alpha = 0^\circ$, the trajectories exhibit inclined enclosed loop shapes, which are slightly disordered. At $5 \leq U_r \leq 7$, more chaotic trajectories are observed. For $10 \leq U_r \leq 13$, the trajectories become regular and exhibit the inclined enclosed loop shapes. When two cylinders are arranged at $\alpha = 90^\circ$, the trajectories are not strictly symmetrical along the cross-flow direction and present a certain inclination, which indicates that the presence of small cylinder has significant effects on the vibration response of the large cylinder. The X-Y trajectories for $\alpha = 180^\circ$ with d/D = 0.3 are shown in Figure 9. An irregular and chaotic circular trajectory is observed at $U_r = 2$. The figure of "8" trajectories are observed

at $4 \leq U_r \leq 7$. Moreover, the trajectories exhibit the enclosed loop shape and become more chaotic at high reduced velocities $U_r \geq 10$.

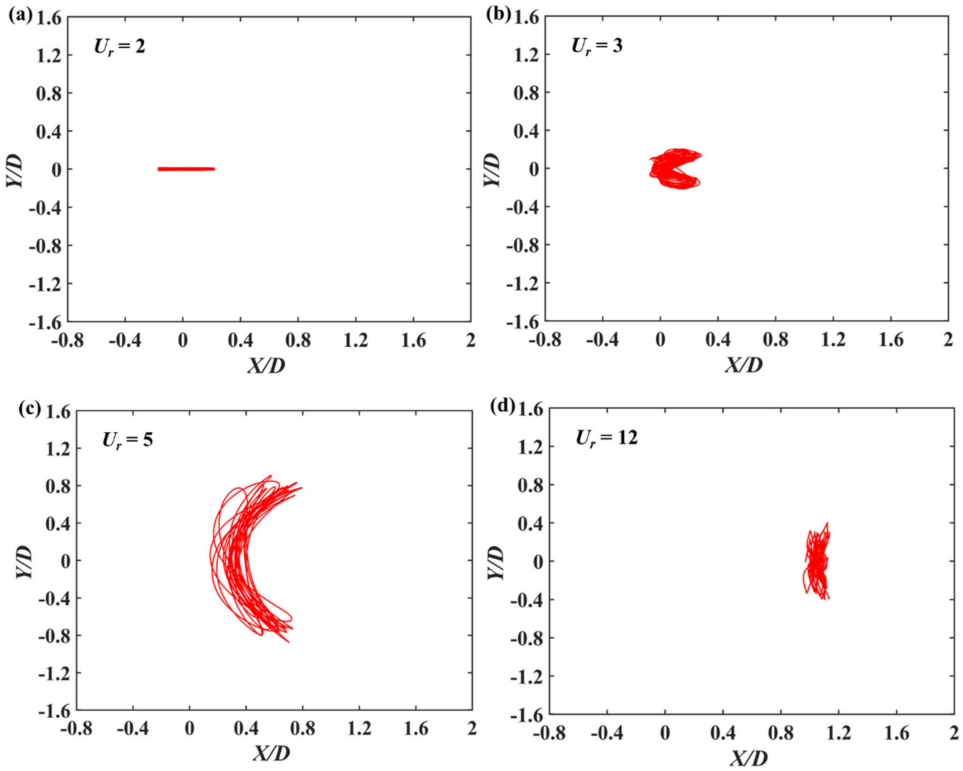

Figure 7. X-Y trajectory of two coupled cylinders at $\alpha = 0°$ and $d/D = 0.3$: (**a**) $U_r = 2$; (**b**) $U_r = 3$; (**c**) $U_r = 5$; (**d**) $U_r = 12$.

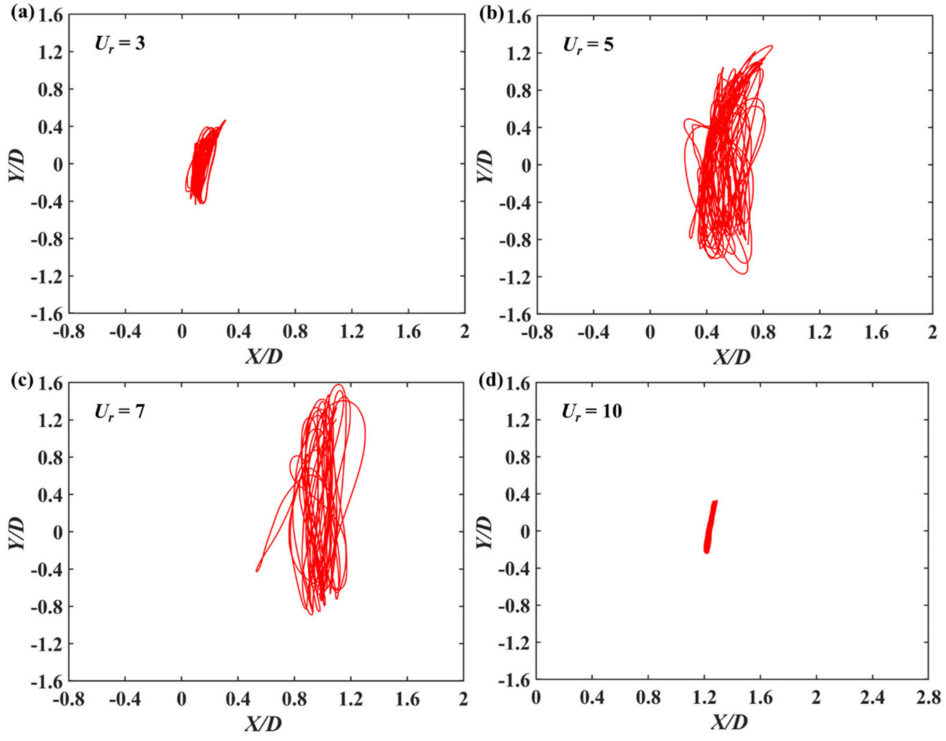

Figure 8. X-Y trajectory of two coupled cylinders at $\alpha = 90°$ and $d/D = 0.3$: (**a**) $U_r = 3$; (**b**) $U_r = 5$; (**c**) $U_r = 7$; (**d**) $U_r = 10$.

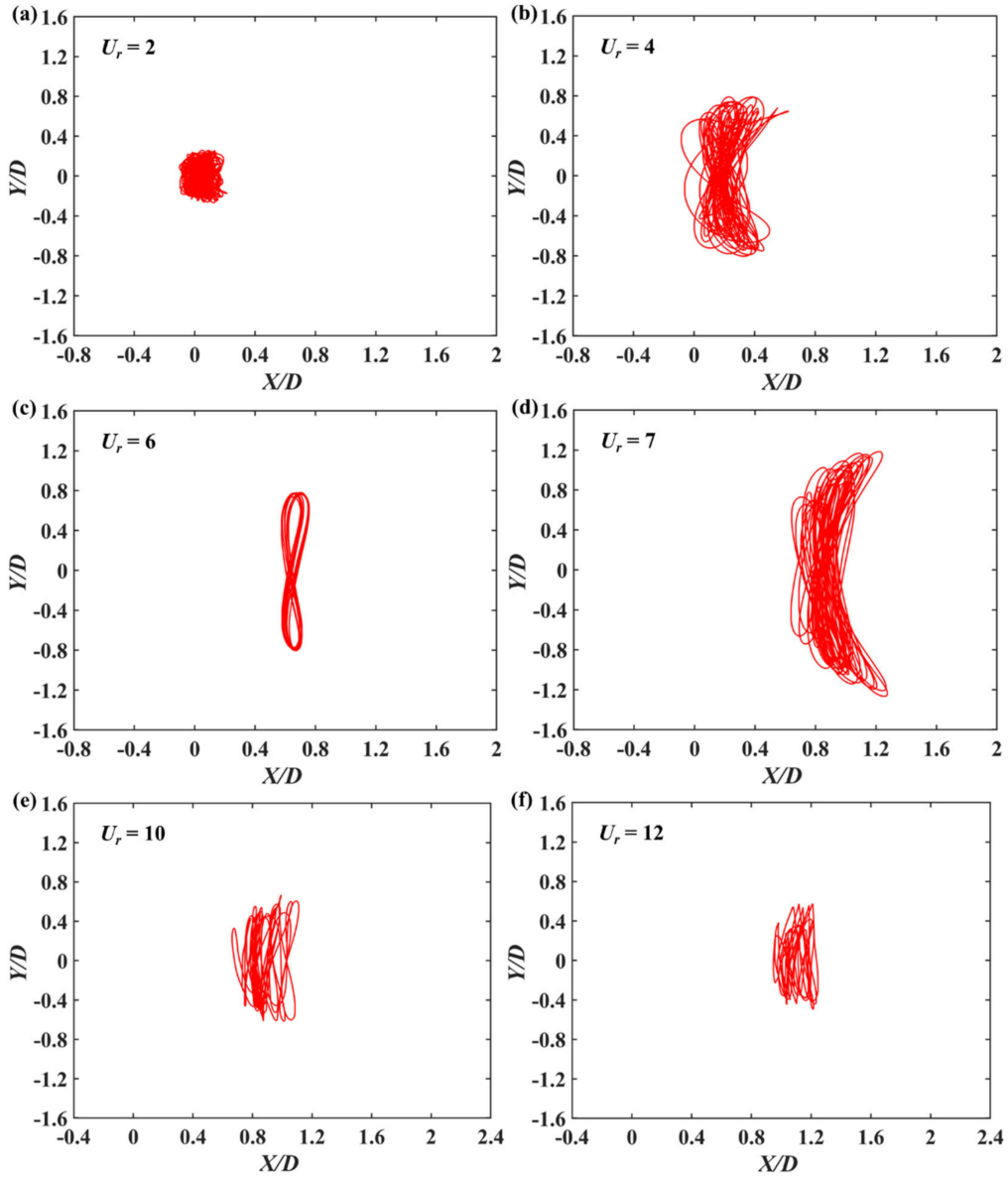

Figure 9. X-Y trajectory of two coupled cylinders at $\alpha = 180^\circ$ and $d/D = 0.3$: (**a**) $U_r = 2$; (**b**) $U_r = 4$; (**c**) $U_r = 6$; (**d**) $U_r = 7$; (**e**) $U_r = 10$; (**f**) $U_r = 12$.

To investigate the effect of diameter ratios on the motion trajectory responses of two coupled cylinders, the X-Y trajectories of two coupled cylinders for $d/D = 0.05$ at $\alpha = 0^\circ$ with different reduced velocities are shown in Figure 10. Different from the complex and disordered trajectories shown in Figures 7–9, the trajectories for small diameter ratio $d/D = 0.05$ behave in a more regular manner. The trajectories of two cylinders resemble the flattened shape of "8" at $U_r = 3$. As the reduced velocity U_r increases to 4 and 5, the trajectories become a little chaotic, but show obvious figures of "8". The dynamic response of the system in the lock-in region is disturbed slightly due to the presence of small cylinder. At $U_r \geq 6$, the trajectory behaves as an obvious figure of "8". As U_r increases to 13, the transverse vibration amplitude decreases significantly.

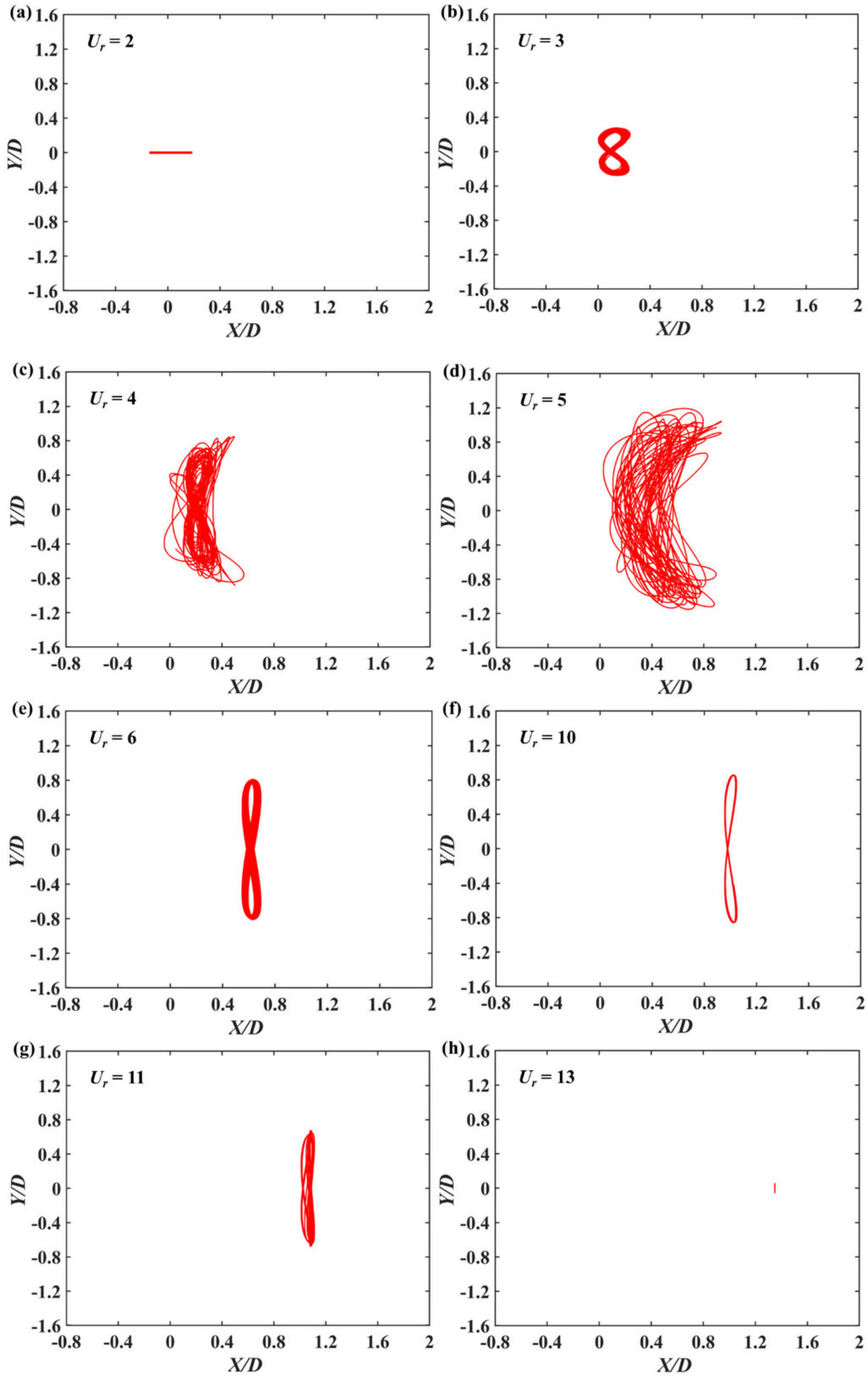

Figure 10. X-Y trajectory of two coupled cylinders at $\alpha = 0^\circ$ and $d/D = 0.05$: (**a**) $U_r = 2$; (**b**) $U_r = 3$; (**c**) $U_r = 4$; (**d**) $U_r = 5$; (**e**) $U_r = 6$; (**f**) $U_r = 10$; (**g**) $U_r = 11$; (**h**) $U_r = 13$.

3.4. Wake Flow Pattern

Figures 11–13 show the instantaneous vorticity contours behind two coupled cylinders with d/D = 0.3 at different incident angles. The incident angle and reduced velocity play important roles in the wake flow pattern behind two coupled cylinders.

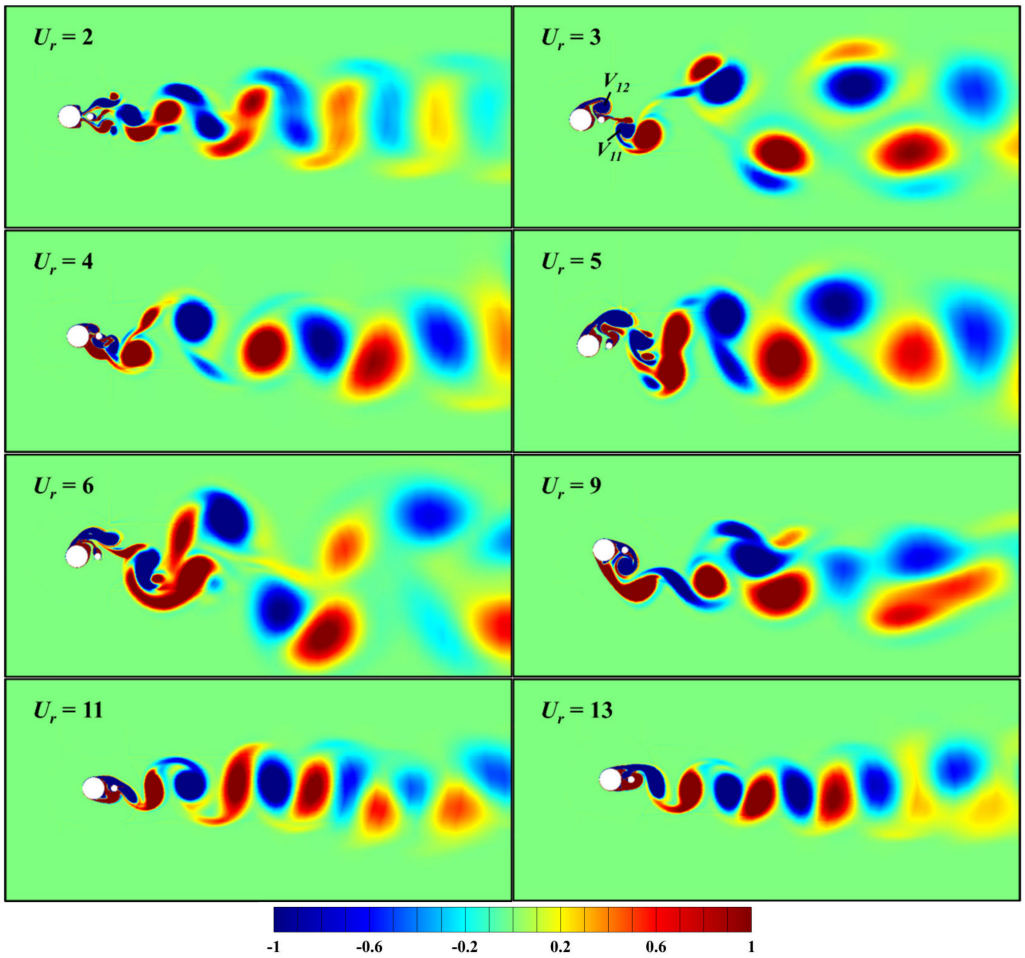

Figure 11. Instantaneous vorticity field for two coupled cylinders at $\alpha = 0°$ and d/D = 0.3.

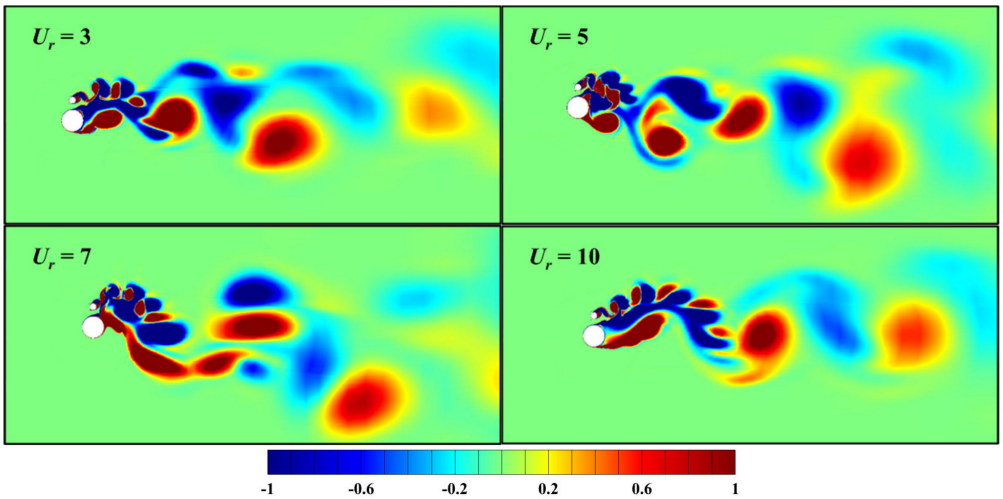

Figure 12. Instantaneous vorticity field for two coupled cylinders at $\alpha = 90°$ and d/D = 0.3.

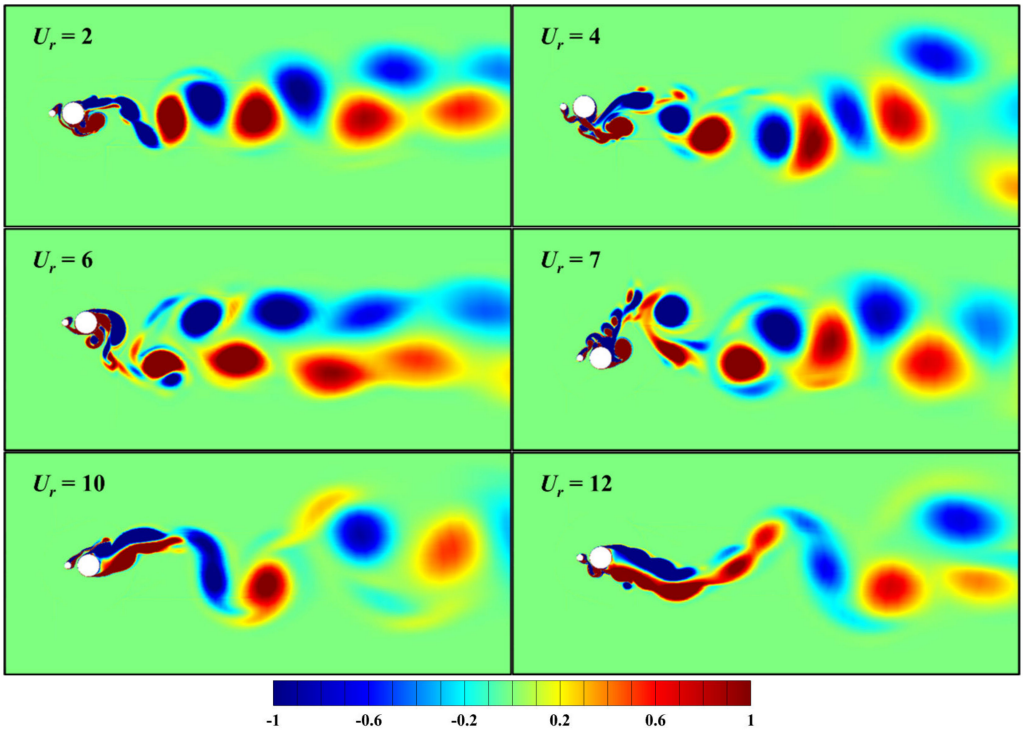

Figure 13. Instantaneous vorticity field for two coupled cylinders at $\alpha = 180^\circ$ and $d/D = 0.3$.

At $\alpha = 0^\circ$, the vortices shedding from the large cylinder impinge on the small cylinder and separate on the top and bottom sides due to the dominant streamwise motion at $U_r = 2$. The vortex shedding mode in the far wake is similar to 2S mode. When U_r increases to 3, a negative vortex from the large cylinder divides into two small vortices during the formation process, leading to a "2P" vortex shedding mode. Then the wake flow pattern becomes 2S mode at $U_r = 4$. As the reduced velocity further increases to $6 \leq U_r \leq 9$, the vortices shedding become more complicated. Moreover, the typical and regular vortex shedding pattern of VIV is not observed, leading to the significant chaotic motions of two coupled cylinders. An obvious 2S mode is observed at high reduced velocities $11 \leq U_r \leq 13$.

For the case of $d/D = 0.3$ and $\alpha = 90^\circ$, the presence of the small cylinder plays an important role on the vortex shedding from the large cylinder, resulting in a more complex and chaotic flow field. The vortices shedding from two coupled cylinders are amalgamated. A pair of vortices is shed from the rear side of the two coupled cylinders and a triplet or quadruplet is observed on the upside. The wake flow pattern is significantly irregular at different reduced velocities. For $\alpha = 180^\circ$ shown in Figure 13, the wake flow pattern can be classified as 2S at $U_r \leq 4$. As U_r increases to 7, similar to the case of $\alpha = 90^\circ$, the vortex shedding from the surface of small cylinder is amalgamated with the shear layer on the upper side of large cylinder. The vortices shed from the small cylinder significantly affect the vortex shedding pattern of two coupled cylinders. For $U_r \geq 10$, the vortices attach to the surface of the large cylinder for a long period and the vortex formation length increases compared with $U_r \leq 9$, which indicates that the transverse displacement decreases with slower separation of shear layer.

For the case of $d/D = 0.05$ and $\alpha = 0^\circ$ as shown in Figure 14, with the decrease in the diameter ratio, the flow field becomes more regular. A symmetric pair of vortices is observed at $U_r = 2$. As U_r increases to $3 \leq U_r \leq 4$, a 2S mode is observed obviously. For $U_r = 5$, the flow field becomes slightly irregular, and the vortex pattern is similar to a P+S mode. The vortices shed from the small cylinder suppress the normal formation and development of vortices shed from the large cylinder. As the reduced velocity further increases to $6 \leq U_r \leq 10$, the vortex pattern becomes a 2P mode, corresponding to the lower branch. With the increase in reduced velocities, the vortex shedding pattern changes to a

2S mode for $U_r \geq 13$. The variation in the wake flow patterns of two coupled cylinders is similar to that of an isolated cylinder, which indicates that the effect of small cylinder on the coupled system becomes weakened with the decrease in the diameter ratio.

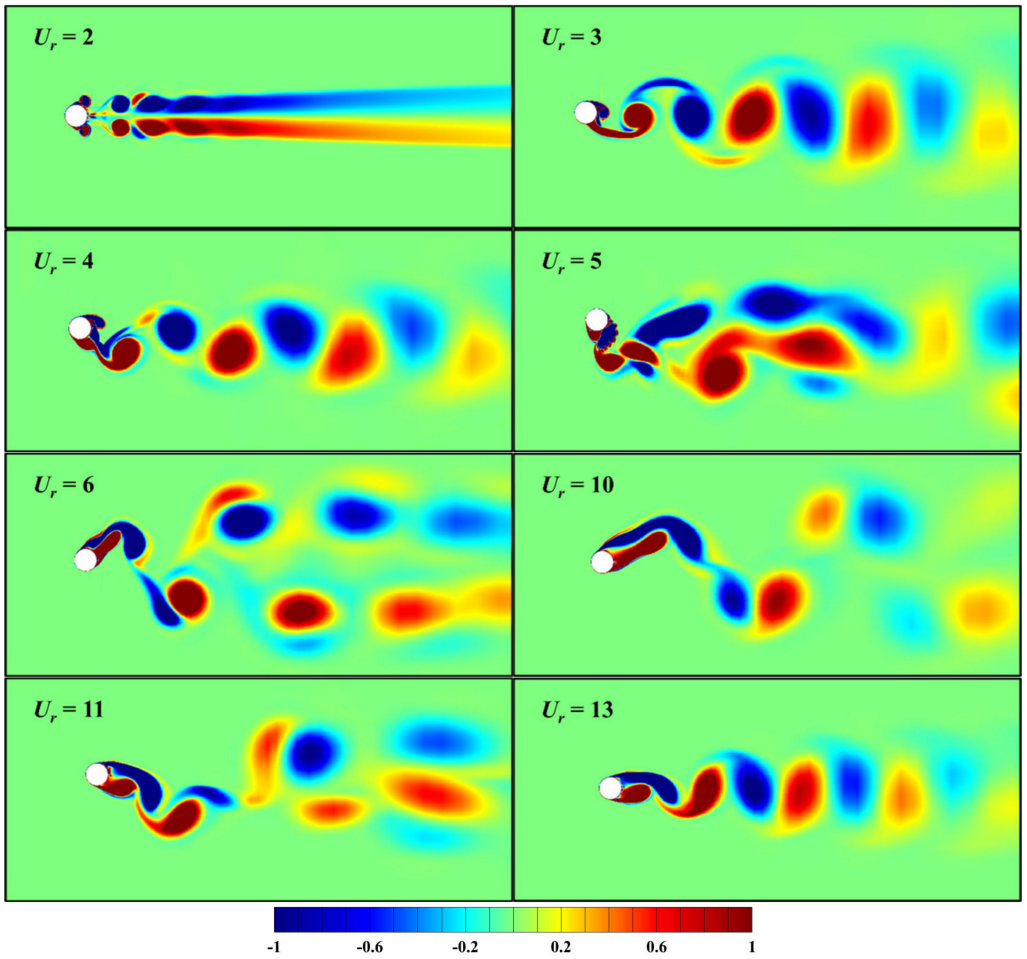

Figure 14. Instantaneous vorticity field for two coupled cylinders at $\alpha = 0°$ and $d/D = 0.05$.

In order to provide a better understanding of the flow topology modifications induced by a small cylinder, the instantaneous vorticity fields in one vibration period T are further analyzed. The instantaneous vorticity contours for $d/D = 0.3$, $\alpha = 0°$ and $U_r = 5$ are presented in Figure 15. At $Ut/D = 300.8$, the positive vortices are shed from the bottom side of the large cylinder surface. At $Ut/D = 302.4$, the negative vortices shed from the large cylinder surface are merged with those shed from the small cylinder. The appearance of the negative vortices below the cylinders complicates the variations in the lift force coefficients of two coupled cylinders, leading to a slightly disordered figure of "8". The flow field and dynamic response become complicated with the presence of the small cylinder.

For $d/D = 0.3$, $\alpha = 90°$, and $U_r = 10$, more complex interactions are observed in Figure 16. Since the gap distance between two cylinders is sufficiently large the drop-off of the shear layer is not directly affected by large cylinder. It can be seen from the time histories of Y-displacement and C_L, two cylinders have four lift periods in one vibration period, leading to the large positive vortex in the rear of large cylinder consisting of four small vortices. Moreover, the large period is consistent with the vibration period. A typical galloping phenomenon is observed at a remarkably lower frequency with respect to the vortex shedding frequency. The vibration of the coupled two-cylinder system in one cycle is affected by the combination of four pairs of vortices. At $Ut/D = 347.4$ and 349.3, three or four pairs of vortices shed from the small cylinder are mixed with the vortex on the top

side of the large cylinder and the vortex formation length of the large cylinder increases due to the presence of the small cylinder, resulting into the smaller vortex intensity on the top side than that on the bottom.

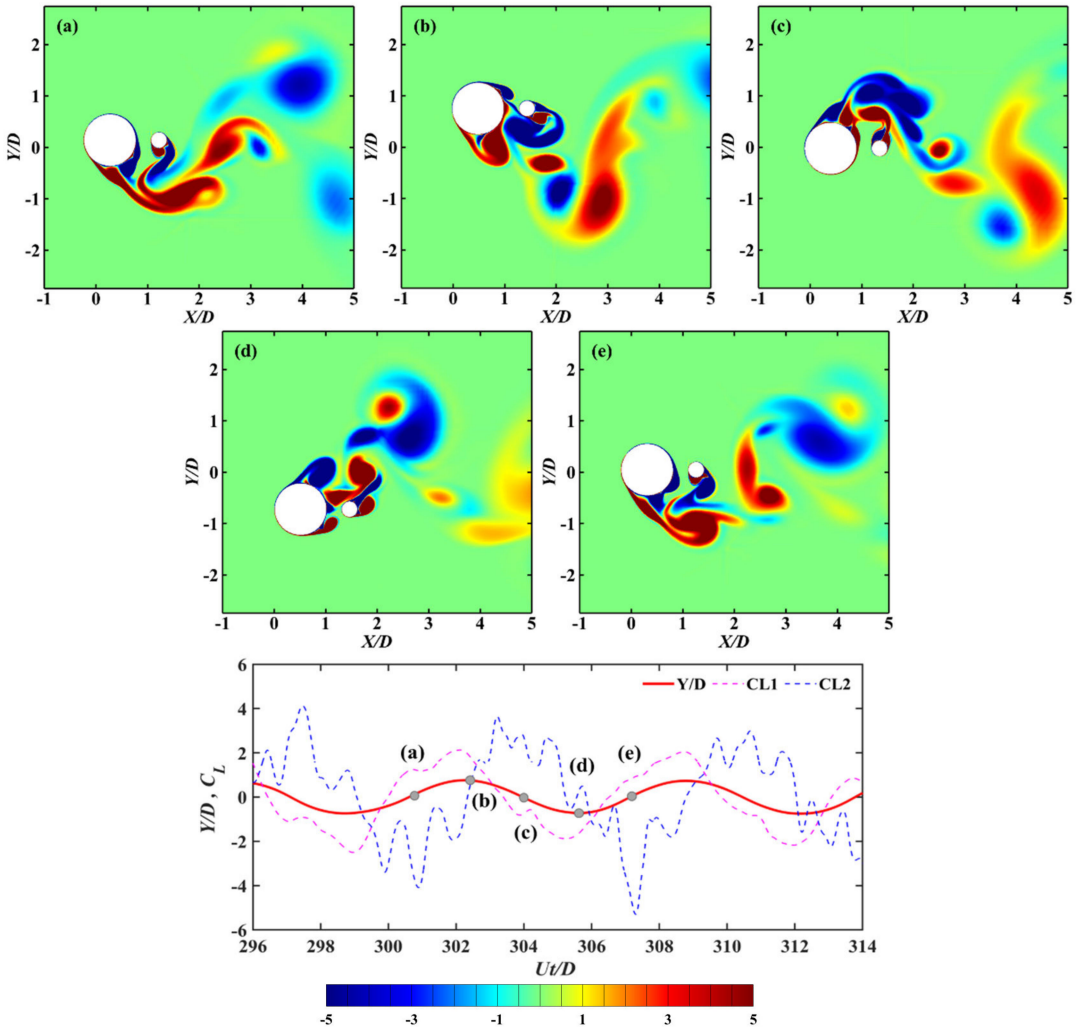

Figure 15. Instantaneous vorticity contours for the typical time instants in one vibration period at d/D = 0.3, α = 0° and U_r = 5: (**a**) Ut/D = 300.8; (**b**) Ut/D = 302.4; (**c**) Ut/D = 304.0; (**d**) Ut/D = 305.6; (**e**) Ut/D = 307.2.

The instantaneous vorticity contours for d/D = 0.05, α = 0°, and U_r = 6 are shown in Figure 17. When two coupled cylinders move to the uppermost position, a pair of vortices is formed above small cylinder and interact with the upper shear layer of large cylinder. The vortices shed from the two lateral sides of the small cylinder with opposite sign are canceled out, resulting in the drag coefficients of small cylinder being almost zero. As can be seen from Figure 17b–d, the small cylinder is always surrounded by vortices of the large cylinder when the cylinders move from the uppermost position to the lowest position. The vortex pattern of the coupled cylinders is similar to that of a single cylinder, and the coupled cylinders can be regarded as a single bluff body. Although the vortex shedding of the large cylinder appears not to be significantly affected by small cylinder, the presence of small cylinder has an effect on the fluctuation of the lift coefficients of two cylinders.

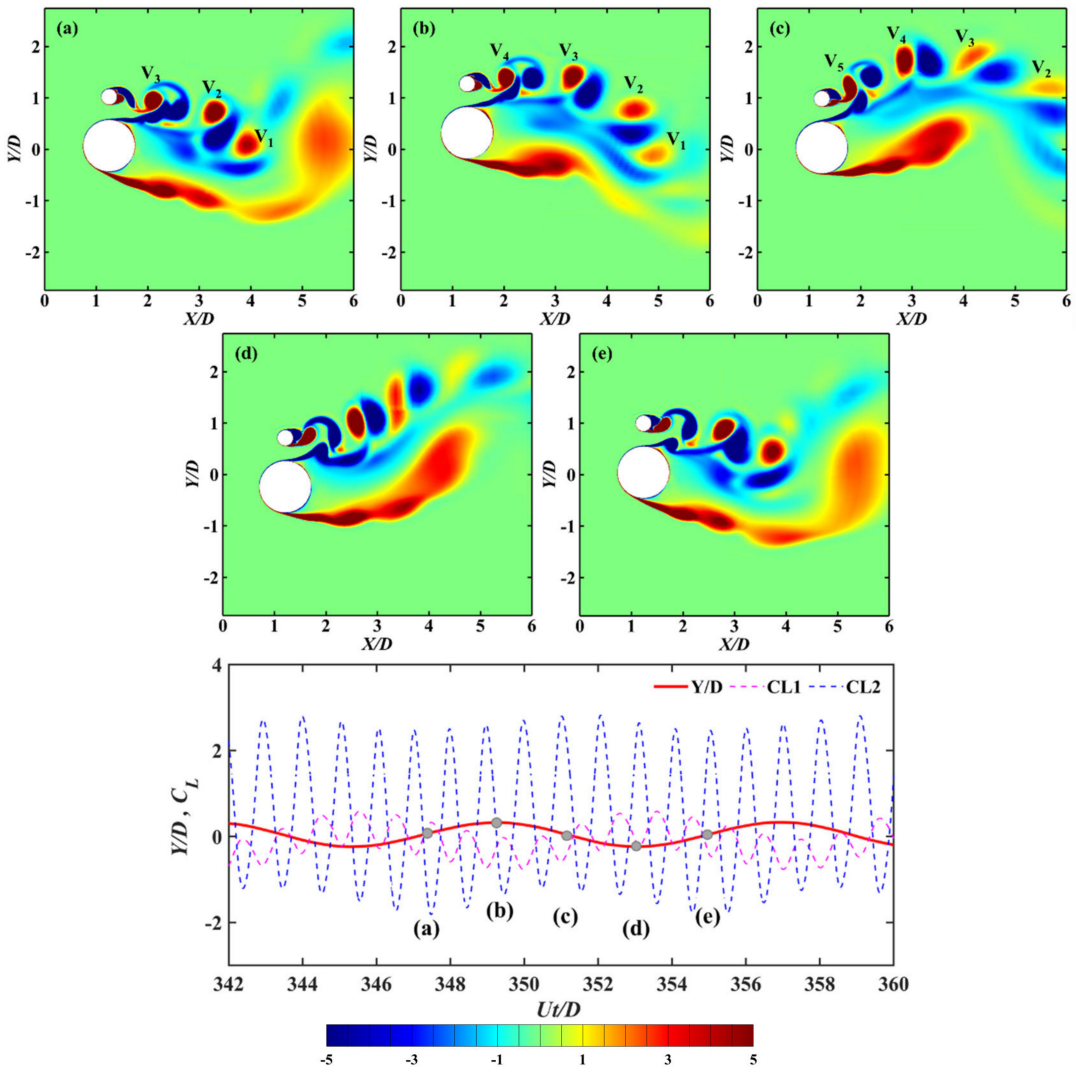

Figure 16. Instantaneous vorticity contours for the typical time instants in one vibration period at d/D = 0.3, $\alpha = 90^{\circ}$, and U_r = 10: (**a**) Ut/D = 347.4; (**b**) Ut/D = 349.3; (**c**) Ut/D = 351.2; (**d**) Ut/D = 353.1; (**e**) Ut/D = 355.0.

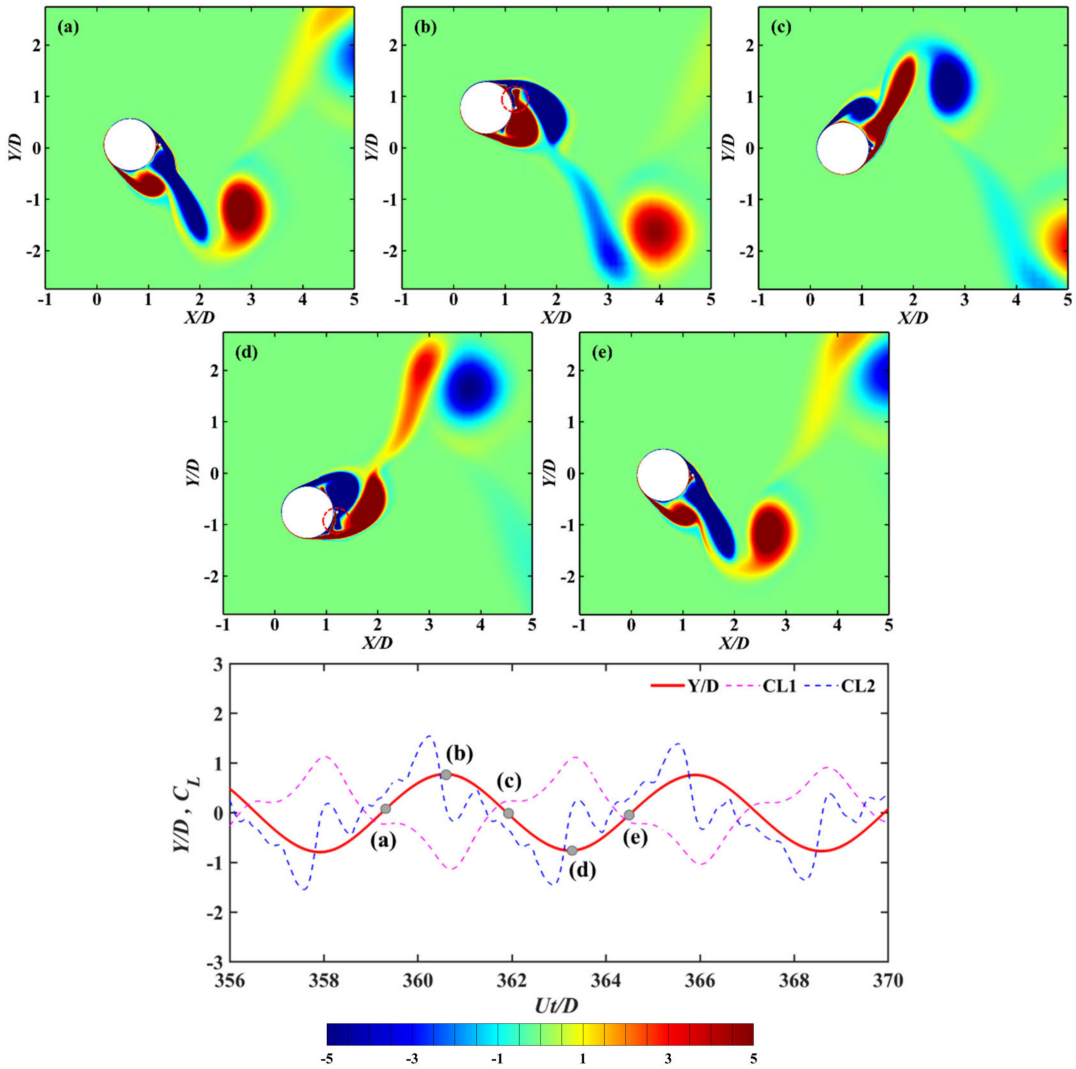

Figure 17. Instantaneous vorticity contours for the typical time instants in one vibration period at d/D = 0.05, α = 0°, and U_r = 6: (**a**) Ut/D = 359.3; (**b**) Ut/D = 360.6; (**c**) Ut/D = 361.9; (**d**) Ut/D = 363.2; (**e**) Ut/D = 364.5.

4. Conclusions

Numerical simulations on two-degree-of-freedom vortex-induced vibration of two coupled cylinders with unequal diameters were performed at Reynolds number Re = 20,000. The effects of the incident angle, diameter ratio, spacing ratio, and reduced velocity on the VIV responses were investigated. The conclusions are summarized as follows:

(1) The range of the lock-in region of two coupled cylinders is widened significantly compared with that of the isolated cylinder. The maximum vibration amplitude decreases due to the presence of small cylinder. The differences in the vibration amplitudes and frequency ratios are particularly pronounced at high reduced velocities especially for α = 0°. The differences become smaller with the decrease in diameter ratio. For the configuration of α = 0°, d/D = 0.05, and G/D = 0.05, the variations in vibration amplitudes and frequency ratios become similar to those of the isolated cylinder.

(2) For all configurations, the variations in mean drag coefficients and root mean square force coefficients of the large cylinder do not vary significantly with the incident angle and diameter ratio, but the force coefficients of small cylinder behave significantly different from those of the isolated cylinder. For the configuration of d/D = 0.3 and α = 0°, the mean drag coefficient of small cylinder is positive in the lock-in regime

and becomes negative outside the lock-in regime. As d/D decreases to 0.05, the mean drag force coefficient of small cylinder almost approaches 0. For $\alpha = 0^\circ$, the mean drag coefficients of two cylinders both decrease slightly as the diameter ratio decreases.

(3) The correlation between the transverse vibration amplitude and lift force coefficients of two coupled cylinders becomes very weak with the increase in diameter ratio and spacing ratio, especially for $U_r \geq 11$ at $d/D = 0.3$. The motion trajectories behave irregular at $\alpha = 90^\circ$ and $d/D = 0.3$ and become regular with the figure of "8" at $\alpha = 0^\circ$ and $d/D = 0.05$.

(4) The presence of the small cylinder has a significant effect on the vortex shedding modes for the large cylinder especially for $\alpha = 90^\circ$ and 180°, different vortex shedding modes such as 2S mode, P+S mode, and 2P mode are observed for two coupled cylinders at different reduced velocities for all investigated configurations. For the case of $d/D = 0.05$, $G/D = 0.05$, and $\alpha = 0^\circ$, the vortex shedding from the large cylinder is not significantly affected.

Author Contributions: Y.G. Conceptualization, Numerical simulation, Supervision, Investigation, Writing-review and editing; S.Y. Numerical model, Numerical simulation, Data curation, Investigation, Writing-original draft preparation; L.W. writing-review and editing; C.H. writing-review and editing; J.Z. writing-review and editing. All authors have read and agreed to the published version of the manuscript.

Funding: This research was funded by the Major Science and Technology Project of Sanya (No. SKJC-2020-01-016) and the Fundamental Research Funds for the Central Universities(No. 226-2022-00171), Sanya Yazhou Bay Science and Technology City was acknowledged.

Institutional Review Board Statement: Not applicable.

Informed Consent Statement: Not applicable.

Data Availability Statement: The data presented in this study are available on request.

Acknowledgments: This research was supported by the Major Science and Technology Project of Sanya (No. SKJC-2020-01-016) and the Fundamental Research Funds for the Central Universities (No. 226-2022-00171), Sanya Yazhou Bay Science and Technology City is acknowledged. Thanks to those who provided support and encouragements to the author during the writing process.

Conflicts of Interest: The authors declare no conflict of interest.

References

1. Wang, J.; Fu, S.; Baarholm, R.; Wu, J.; Larsen, C.M. Fatigue damage of a steel catenary riser from vortex-induced vibration caused by vessel motions. *Mar. Struct.* **2014**, *39*, 131–156. [CrossRef]
2. Jauvtis, N.; Williamson, C.H.K. The effect of two degrees of freedom on vortex-induced vibration at low mass and damping. *J. Fluid Mech.* **2004**, *509*, 23–62. [CrossRef]
3. Wu, X.; Ge, F.; Hong, Y. A review of recent studies on vortex-induced vibrations of long slender cylinders. *J. Fluids Struct.* **2012**, *28*, 292–308. [CrossRef]
4. Kang, Z.; Ni, W.; Sun, L. A numerical investigation on capturing the maximum transverse amplitude in vortex induced vibration for low mass ratio. *Mar. Struct.* **2017**, *52*, 94–107. [CrossRef]
5. Han, X.; Lin, W.; Wang, D.; Qiu, A.; Feng, Z.; Tang, Y.; Wu, J. Numerical simulation of super upper branch of a cylindrical structure with a low mass ratio. *Ocean Eng.* **2018**, *168*, 108–120. [CrossRef]
6. Feng, C.C. The Measurement of Vortex-Induced Effects in Flow Past Stationary and Oscillating Circular and D-Section Cylinders. Master's Thesis, University of British Columbia, Vancouver, BC, Canada, 1968.
7. Khalak, A.; Williamson, C.H.K. Motions, forces and mode transitions in vortex-induced vibrations at low mass-damping. *J. Fluids Struct.* **1999**, *13*, 813–851. [CrossRef]
8. Verma, M.; De, A. Three-dimensionality in the flow of an elastically mounted circular cylinder with two-degree-of-freedom vortex-induced-vibrations. *Phys. Fluids* **2022**, *34*, 103616. [CrossRef]
9. Jauvtis, N.; Williamson, C.H.K. Vortex-induced vibration of a cylinder with two degrees of freedom. *J. Fluids Struct.* **2003**, *17*, 1035–1042. [CrossRef]
10. Blevins, R.D.; Coughran, C.S. Experimental Investigation of Vortex-Induced Vibration in One and Two Dimensions With Variable Mass, Damping, and Reynolds Number. *J. Fluids Eng.* **2009**, *131*, 101202. [CrossRef]

11. Borazjani, I.; Sotiropoulos, F. Vortex-induced vibrations of two cylinders in tandem arrangement in the proximity–wake interference region. *J. Fluid Mech.* **2009**, *621*, 321–364. [CrossRef]
12. Ping, H.; Cao, Y.; Zhang, K.; Han, Z.; Zhou, D.; Zhu, H.; Bao, Y. Vortex-induced vibrations of two rigidly coupled circular cylinders in tandem arrangement. *Ocean Eng.* **2022**, *263*, 112316. [CrossRef]
13. Papaioannou, G.V.; Yue, D.K.P.; Triantafyllou, M.S.; Karniadakis, G.E. On the effect of spacing on the vortex-induced vibrations of two tandem cylinders. *J. Fluids Struct.* **2008**, *24*, 833–854. [CrossRef]
14. Chung, M.-H. On characteristics of two-degree-of-freedom vortex induced vibration of two low-mass circular cylinders in proximity at low Reynolds number. *Int. J. Heat Fluid Flow* **2017**, *65*, 220–245. [CrossRef]
15. Chen, W.; Ji, C.; Xu, D. Vortex-induced vibrations of two side-by-side circular cylinders with two degrees of freedom in laminar cross-flow. *Comput. Fluids* **2019**, *193*, 104288. [CrossRef]
16. Chen, W.; Ji, C.; Xu, D.; An, H.; Zhang, Z. Flow-induced vibrations of two side-by-side circular cylinders at low Reynolds numbers. *Phys. Fluids* **2020**, *32*, 023601. [CrossRef]
17. Zang, Z.; Gao, F. Vortex shedding and vortex-induced vibration of piggyback pipelines in steady currents. In Proceedings of the Twenty-Second International Offshore and Polar Engineering Conference, Rhodes, Greece, 17–22 June 2012.
18. Zang, Z.-P.; Gao, F.-P. Steady current induced vibration of near-bed piggyback pipelines: Configuration effects on VIV suppression. *Appl. Ocean Res.* **2014**, *46*, 62–69. [CrossRef]
19. Assi, G.R.S. Wake-induced vibration of tandem and staggered cylinders with two degrees of freedom. *J. Fluids Struct.* **2014**, *50*, 340–357. [CrossRef]
20. Zhao, M.; Cheng, L.; Teng, B.; Liang, D. Numerical simulation of viscous flow past two circular cylinders of different diameters. *Appl. Ocean Res.* **2005**, *27*, 39–55. [CrossRef]
21. Zhu, H.; Tan, X.; Gao, Y.; Zhou, T.; Liu, W. Two-degree-of-freedom flow-induced vibration of two rigidly coupled tandem cylinders of unequal diameters. *Ocean Eng.* **2020**, *216*, 108142. [CrossRef]
22. Zhao, M.; Murphy, J.M.; Kwok, K. Numerical Simulation of Vortex-Induced Vibration of Two Rigidly Connected Cylinders in Side-by-Side and Tandem Arrangements Using RANS Model. *J. Fluids Eng.* **2015**, *138*, 021102. [CrossRef]
23. Zhao, M.; Yan, G. Numerical simulation of vortex-induced vibration of two circular cylinders of different diameters at low Reynolds number. *Phys. Fluids* **2013**, *25*, 083601. [CrossRef]
24. Rahmanian, M.; Zhao, M.; Cheng, L.; Zhou, T. Two-degree-of-freedom vortex-induced vibration of two mechanically coupled cylinders of different diameters in steady current. *J. Fluids Struct.* **2012**, *35*, 133–159. [CrossRef]
25. Rahmanian, M.; Cheng, L.; Zhao, M.; Zhou, T. Lock-in study of two side-by-side cylinders of different diameters in close proximity in steady flow. *J. Fluids Struct.* **2014**, *49*, 386–411. [CrossRef]
26. Serta, C.P.V.; Janocha, M.J.; Yin, G.; Ong, M.C. Numerical simulations of flow-induced vibrations of two rigidly coupled cylinders with uneven diameters in the upper transition Reynolds number regime. *J. Fluids Struct.* **2021**, *105*, 103332. [CrossRef]
27. Ping, H.; Zhu, H.; Zhang, K.; Zhou, D.; Bao, Y.; Han, Z. Vortex-induced vibrations of two rigidly coupled circular cylinders of unequal diameters at low Reynolds number. *Phys. Fluids* **2021**, *33*, 103603. [CrossRef]
28. Wanderley, J.B.V.; Souza, G.H.B.; Sphaier, S.H.; Levi, C. Vortex-induced vibration of an elastically mounted circular cylinder using an upwind TVD two-dimensional numerical scheme. *Ocean Eng.* **2008**, *35*, 1533–1544. [CrossRef]
29. Govardhan, R.N.; Williamson, C.H.K. Defining the 'modified Griffin plot' in vortex-induced vibration: Revealing the effect of Reynolds number using controlled damping. *J. Fluid Mech.* **2006**, *561*, 147–180. [CrossRef]
30. Wanderley, J.B.V.; Soares, L.F.N. Vortex-induced vibration on a two-dimensional circular cylinder with low Reynolds number and low mass-damping parameter. *Ocean Eng.* **2015**, *97*, 156–164. [CrossRef]
31. Gsell, S.; Bourguet, R.; Braza, M. Two-degree-of-freedom vortex-induced vibrations of a circular cylinder at Re = 3900. *J. Fluids Struct.* **2016**, *67*, 156–172. [CrossRef]
32. Gao, Y.; Zhang, Y.; Zhao, M.; Wang, L. Numerical investigation on two degree-of-freedom flow-induced vibration of three tandem cylinders. *Ocean Eng.* **2020**, *201*, 107059. [CrossRef]
33. Gao, Y.; Yang, K.; Zhang, B.; Cheng, K.; Chen, X. Numerical investigation on vortex-induced vibrations of four circular cylinders in a square configuration. *Ocean Eng.* **2019**, *175*, 223–240. [CrossRef]